ADVANCED MATERIALS INTERFACES
www.advmatinterfaces.de

# Real-Space Observation of Potential Reconstruction at Metallic/Insulating Oxide Interface

*Qingxuan Jia and Alexandre Gloter**

**Electric field reconstruction at interfaces plays a crucial role in device performances controlling, for example, Schottky potential barrier and interfacial Rashba effect. Here, scanning transmission electron microscopy (STEM) and ab-initio calculation are used to estimate the atomic-scale and large-scale potential reconstruction at the interface between a metallic oxide $SrRuO_3$ (SRO) thin film and an insulating $DyScO_3$ (DSO) substrate. The intensity and the symmetry of the large-scale electrostatic reconstruction at the interface is probed by 4D-STEM discussing the center-of-mass shift for different angular ranges detection. Numerical simulations indicate that thermal diffuse scattered (TDS) electrons can be sensitive to large-scale electric field and experiments based on these diffused electrons near the interface confirm that the electric field extends more in the insulating $DyScO_3$ (DSO) side. The magnitude of the electrostatic drop at the interface estimated by the 4D-STEM experiment is in accordance with the ab-initio values for a p-type reconstruction of the interface plane. Furthermore, an atomically resolved TDS potential asymmetry is observed in real-space at the SRO/DSO interface by 4D-STEM. This asymmetry is associated with the formation of a local ferroelectric type dipole at the interfacial unit-cell revealing unambiguously the balance evolution between antiferrodistortive and ferroelectric instabilities at the interface between a metallic SRO and an insulating DSO.**

## 1. Introduction

Interfaces play a crucial role in device performance controlling, for example, Schottky potential barrier[1] or interfacial Rashba effect.[2] In case of oxide heterostructures, the potential discontinuity at the interface can greatly vary depending on the bulk electronic structures but also the plane termination, the atomic reconstruction, the valence distribution, and the interdiffusion. Techniques allowing simultaneous structural and potential determination at interfaces will thus meet a great need. Scanning transmission electron microscopy (STEM) has played an important role in determining structural aspects at interfaces, notably by imaging heavy atoms and their displacements by high angle annular dark field (HAADF) detection with an accuracy that can be well below 5 pm.[3] More recently, annular bright field (ABF) imaging has extended the STEM imaging capability to light elements such as oxygen,[4] enabling the oxygen octahedral reconstruction at interfaces[5] or in super-lattices[6] to be elucidated.

Meanwhile, 4D-STEM techniques, where a part of the diffraction pattern is collected at every position of the electron probes have strongly developed. Combined with different numerical procedures such as differential phase contrast (DPC) or ptychography, it has enable to improve the contrast in low-dose imaging,[7] the spatial resolution[8] or to visualize magnetic or electric field.[9] The case of electric field imaging, either concerning atomic-scale or longer range modulation, has motivated many recent 4D-STEM works.[10–15] When the electron feels the in-plane electric field contribution of the material, it will suffer a deviation, id est, displacing the center of mass (COM), or the first moment, of the diffraction pattern. Many works have used this COM displacement to image the electric field distribution occurring at the vicinity of the atomic columns due to the screened strong nucleus attraction. Since the electric field measurement by the COM displacement is mostly valid in the weak phase approximation,[16,17] the technique is very adapted for the investigation of thin lamelar materials. The atomic electrostatic maps have thus been obtained for graphene,[13] hexagonal boron nitride[10] and 2D monolayers transition metal dichalchogenide.[12,18] From the differentiation or integration of the electric field, it is possible to retrieve the charge or the

Q. Jia
State Key Laboratory for Superlattices and Microstructures
Institute of Semiconductors
Chinese Academy of Sciences
Beijing 100083, China
Q. Jia
College of Materials Science and Opto-Electronic Technology
University of Chinese Academy of Sciences
Beijing 100049, China
Q. Jia, A. Gloter
Université Paris-Saclay
CNRS
Laboratoire de Physique des Solides
Orsay 91405, France
E-mail: alexandre.gloter@u-psud.fr
The ORCID identification number(s) for the author(s) of this article can be found under https://doi.org/10.1002/admi.202202165.



**DOI: 10.1002/admi.202202165**

potential. In the case of these thin materials, the obtained experimental charges and potentials are in a good agreement with the volumetric data obtained by first principle calculations, including in the case of defects such as vacancy lines in $MoS_2$[12] or nanopores in graphene.[13] It is here to note, that these investigated defects also imply brusque potential discontinuities with spatial variations at the order of the atomic-scale. Such COM based techniques have also been used for bulk sample. The electric field in GaN and $SrTiO_3$ have then been reported using 300 keV electrons while being collected at the thinnest part of the samples (<5 nm).[19] The atomic electric field distribution was also measured for low symmetry $ABO_3$ perovskite. The case of the ferroelectrically distorted $BiFeO_3$[14] and of the antiferrodistortive oxygen-octahedron rotation in $DyScO_3$[15] were successfully reported. For both cases, the sample thickness was below 10 nm. By comparing experimental and calculated 4D-STEM data of $SrTiO_3$, Addiego et al.[11] reported that qualitative electric field can still be measured for sample thickness up to 15 nm. The case of electric field slowly varying over several unit-cells, as encountered at interface or junction, has also been investigated by 4D-STEM. The built-in electric field at a p-n junction in GaAs has been measured using a 0.13 mrad semi-angle probe forming aperture and a corresponding 12 nm spatial resolution.[20] The obtained electric field was in agreement with the expectation taking into account the presence of inactive layers on both surfaces of the STEM lamella. MacLaren et al.[21] also observed a DPC signal at a charged antiphase domain boundary in a doped bismuth ferrite. They point out that, despite the use of a rather low convergence angle of 1.5 mrad resulting in non-overlapping disks, care is required in the interpretation of the DPC signal since diffraction effect can still prevail. Similar cares have been point-out in the case of a COM approach for measuring the electric field across AlN/GaN system.[22,23] While the polarisation induced internal electric field was properly measured, even for lamellae as thick as 110 nm,[23] the electric field associated to the interfaces between the two materials was more difficult to quantify. Indeed, the differences of the mean-inner potential gives rise to a strong COM at the interface between AlN and GaN, but it is also shown that dynamical scattering can redistributed the intensity in such a way that the COM sign can even be reversed.[22] Yang et al.[24] reported the electrostatic characteristic of a grain boundary in a $SrTiO_3$ bi-crystal. They used two sets of collection semi-angles, 20 mrad for atomical resolved electric field investigation and a 6 mrad for the large-scale electric field measurement as encountered next to the grain boundary. The electric field distribution observed by the 4D-STEM was then in agreement with the one expected for a double-Schottky-barrier model and extended over ca. 10 nm.

In this Article, we first evaluate how the COM based atomic images are changing as a function of the collected angles and thicknesses by discussing the cases of a symmetric $SrTiO_3$ (simulation and experiment) and a distorted perovskite, for example, $DyScO_3$ (experiment). We numerically demonstrated that thermal diffuse scattered electrons can be sensitive to large-scale or homogeneous external electric field. We then investigate the potential reconstruction at the interface between a metallic oxide $SrRuO_3$ thin film (SRO) and the insulating $DyScO_3$ substrate (DSO). Both have perovskite structures and are, respectively, used as an oxide electrode and a straining substrate in ferroelectric nano-devices.[25–29] We measured by 4D-STEM the COM components across the interface for different angles and we separate the large-scale and atomic-scale contributions for a further comparison with ab-initio modeling. When estimated on the medium-angle, the intensity of the large-scale electric field is in fair agreement with the calculated potential step. We also observe a TDS based potential asymmetry within the last interfacial unit-cell that is related to the formation of a polar displacement at the last unit-cell. This asymmetry demonstrates unambiguously the balance evolution between antiferrodistortive and ferroelectric instabilities at these oxide interfaces.

## 2. Results and Discussion

**Figure 1**a shows the norms of COM (i.e., the estimation of in-plane electric field intensity) and the corresponding electron phases as obtained by simulating 4D-STEM data of $SrTiO_3$ at different thicknesses. The simulations have been done by computing the COM displacement for different sections of the diffraction pattern corresponding to the bright field disk (BF, 0–30 mrad), the whole pattern (WP, 0-100 mrad) and an intermediate region, mostly corresponding to the so-called medium angle annular dark field imaging (MA, 40-100 mrad). For the BF-COM and WP-COM cases, the atomic electric field distribution stay circular around the columns for thicknesses up to 16 nm confirming the work of Addiego et al.[11] For thicker slabs, the electric field exhibits square like features and several additional nodes occurs, due to the stronger dynamical contribution. The resulting phases deviate strongly from the expected phase distributions, with maxima even being located away from the atomic columns. On the other hand, the momentum transfers associated to the MA-COM exhibit more circular features and the corresponding integration are stable with thickness, keeping optima located at the atomic columns. Such angular region is usually discarded since it corresponds to electron mostly scattered through thermal diffuse scattering (TDS), with a rather negligible total cross-section for thin samples.[30] Furthermore, the origin of these scattered electrons resides in the absorptive part of the potential and is not representative of the atomic electric field around the atoms. The similarity of the images is in fact due to the similar shape of the elastic and TDS inelastic scattering potential near the atoms.[31] Figure 1b shows the COM intensity for the Sr and O columns as a function of the selected angle and thicknesses. All curves exhibit similar trends. The COM first increases for thicknesses up to ca. 5 nm, as already reported.[11] For higher thickness, the COMs show a continuous decay, indicating that the probe intensity has strongly delocalized, further, suffering dynamical effect and that the COM values do not accumulate anymore when propagating through the sample. The intensity of the COM obtained from the MA region is substantially larger than from the BF/WP angles for all thicknesses. The COM ratios between the two types of columns also indicates that the MA-COM exhibit a rather constant ratio (for thickness above 10 nm) avoiding any intensity inversion between the two columns intensities. Similar calculations have been done for electrons propagating

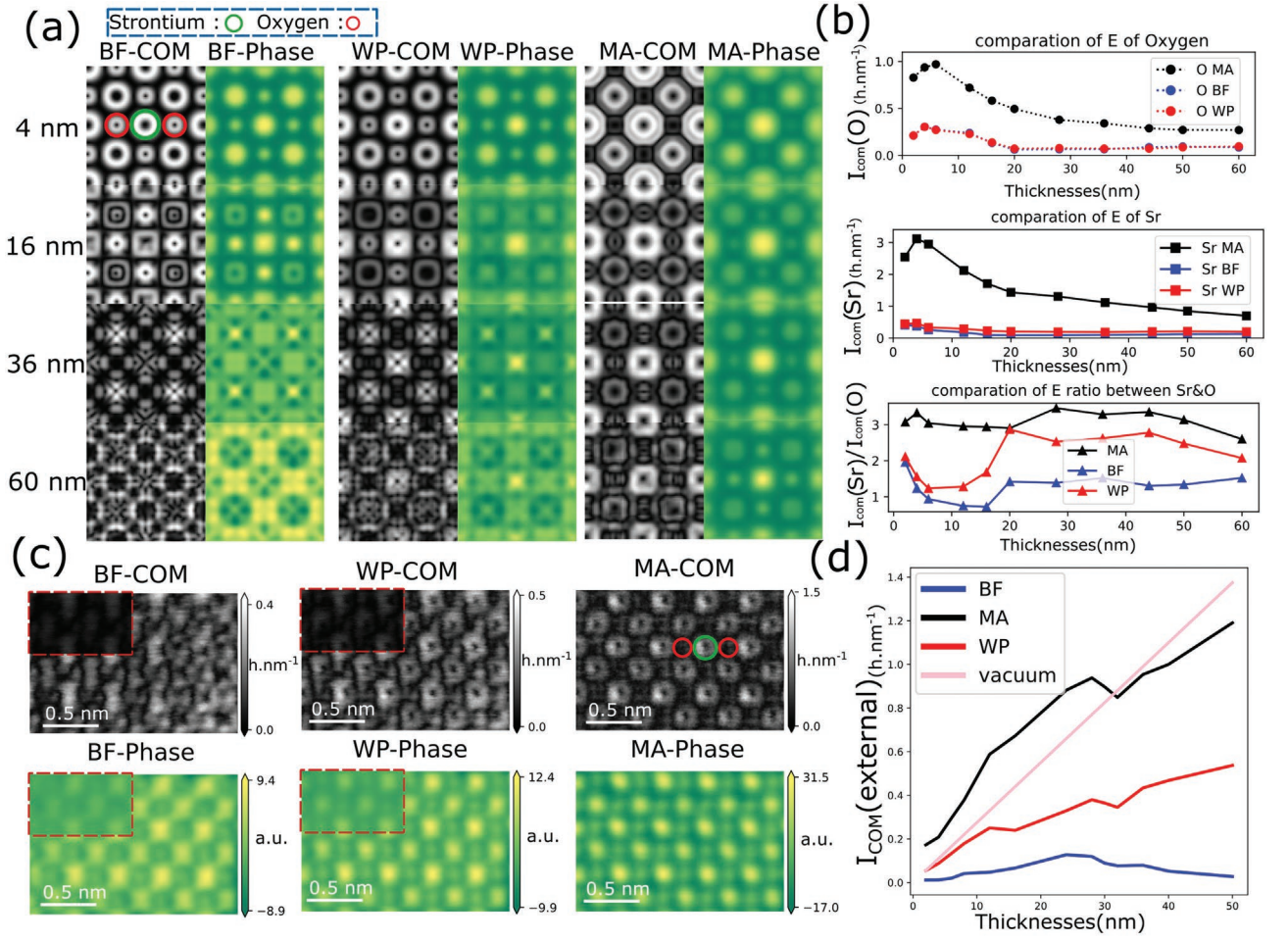


**Figure 1.** a) Calculated COM and phase of $SrTiO_3$ as obtained from different part of the diffraction pattern (BF: 0-30 mrad, WP: 0-100 mrad, MA: 40-100 mrad, for 100 keV electrons). At every thickness, the COM and phase values are completely mapped by the value range of 'greyscale' and 'summer' color map separately. b) Calculated averaged intensity of the COM of the strontium and oxygen columns and their ratios as a function the thickness. The average has been done within the circles indicated in (a) with, respectively, red and green circles for O and Sr columns. c) Experimental COM and phase of $SrTiO_3$ as obtained from different part of the diffraction pattern (BF: 0-30 mrad, WP: 0-100 mrad and MA: 45-90 mrad). The inset parts of the BF and WP figures have been set to the same scale intensity as for the MA figures to clarify their relative intensities. d) Calculated average intensity of the COM due to an external electric field of 5 V $nm^{-1}$ superimposed to the $SrTiO_3$ unit-cell. The straight line corresponds to the BF disk deviation for a similar electric field in the vacuum.

at 200 keV and it shows that the same BF-COM, WP-COM and MA-COM comparison holds for different acceleration voltages (see Figure S1, Supporting Information). Experimental 4D-STEM measurement is reported (Figure 1c) for a $SrTiO_3$ (STO) sample of ca. 40 nm. Three images of the COM intensity have been obtained by selecting the BF (0-30 mrad), WP (0-100 mrad) and MA (45-90 mrad) part of the diffraction pattern. For such thick sample, the BF based COM has very weak intensity and shows no meaningful features. As expected from the numerical simulations, the MA-COM map exhibits optima at the atomic columns, with a more circular distribution. The phase maps retrieved from the three different atomic COM distributions clearly evidence that, qualitative results can also be obtained for thick samples by considering the COM contributions of the electron scattered out the BF disk.

The similarity of the images obtained by estimating the COM at the bright field angles for thin sample and at the medium angles for thick sample is due to the similar shape of the elastic and the absorptive scattering potentials at the vicinity of the nuclei.[31] This similarity also confirms that, while 4D-STEM is theoretically measuring electric field at the atomic-scale, many details on the electronic structures of the materials are often hidden or lost, due various experimental effects, such as the shape of the probe gradient.[32] Nevertheless, while the similarity between the BF and the MA-COM images is on somehow spurious, it can be experimentally useful to collect MA-COM images since they shows a high contrast. A second reason is that the electrons that have been scattered by TDS are not suffering anymore from a strong diffraction process and they might imprint the presence of an homogeneous large-scale electric field while the rest of the electrons is maintaining an atomic-scale resolution. This second point has been tested by numerical simulations where an electric field of an intensity of 5 V $nm^{-1}$ have been superimposed to the $SrTiO_3$ unit-cell (see details of calculation in Figure S2, Supporting Information).[33,34] For such homogeneous electric field (without

the presence of the material), a displacement of the BF disk of 0.275 h $nm^{-1}$ is typically expected for every 10 nm of thickness (for 100 keV electrons). Numerical simulation obtained without the material confirms this value by showing a straight line (Figure 1d). When a material is present, the averaged COM have been calculated by integrating their values over the whole STO unit-cell, here again, for different angles. The averaged COM estimated on the BF has almost no deviation associated to the homogeneous electric field, while the WP-COM imprint part of it. For thicknesses up to 50 nm, and electric field of 5 V $nm^{-1}$, the MA based COM is in fair agreement with the expectations. Many effects play a role such as the amount of TDS scattered electrons at a given thickness or the increased contrast due to the measured COM over an annular geometry.[35] It might explain the overshoot of the MA-COM at low thickness and then a reduction for ca. 50 nm. On the other hand, it seems that measuring the COM displacement associated to TDS scattered electrons might be a complement for measuring the large-scale electric field, to experiments with reduced convergences angles, that furthermore are also not always quantitative.

The atomic-scale electric field maps of a low symmetry $DyScO_3$ perovskite (Pbnm) was also experimentally investigated. In a similar approach, the COM intensities have been measured from the BF, MA and WP angles for two areas corresponding to ca. 33 and 98 nanometers thick lamellae (**Figure 2**a). For both thicknesses, only the COM as estimated from the MA ranges give clear minima at the columns position combined with a rather spherical symmetry around the collumns. The profiles (Figure 2b) obtained across a Dy-OO direction [-110] evidence that the intensity of the COM norm is larger for the MA-COM and that the intensity is decreasing for the thicker sample as expected for such thickness range (>10 nm). The numbers of electron scattered in the MA range is rather weak and the COM images and profiles measured with sub milli-second exposure times are thus noisy. In order to increase the signal-to-noise ratio of the MA-COM map, STEM-4D data have been collected using an hybrid detector with a counting depth limited to 1 bit (see Figure S3, Supporting Information). In such condition, acquisition times down to ca. 0.1 ms can be obtained with non-saturated pixels in the MA range. It is then possible to collect series of 4D-STEM images with on-line spatial drift correction. The image in Figure 2c is acquired following this approach. The 4D-STEM data are collected in ca. 8.5 s (256x256 pixels, 10 pm scanning step) and the final COM maps are obtained after the on-line drift compensation and the summation of a ten of data. The atomic MA-COM maps in Figure 2c (50 nm thick sample) show very resolved features, with sharp minimum at the position of the Dy atoms (and a clear Dy zig-zag chain visible along the [001] axis), in correspondence to the atomic crystal structure. The profile (Figure 2d) extracted across a Dy-O-O series

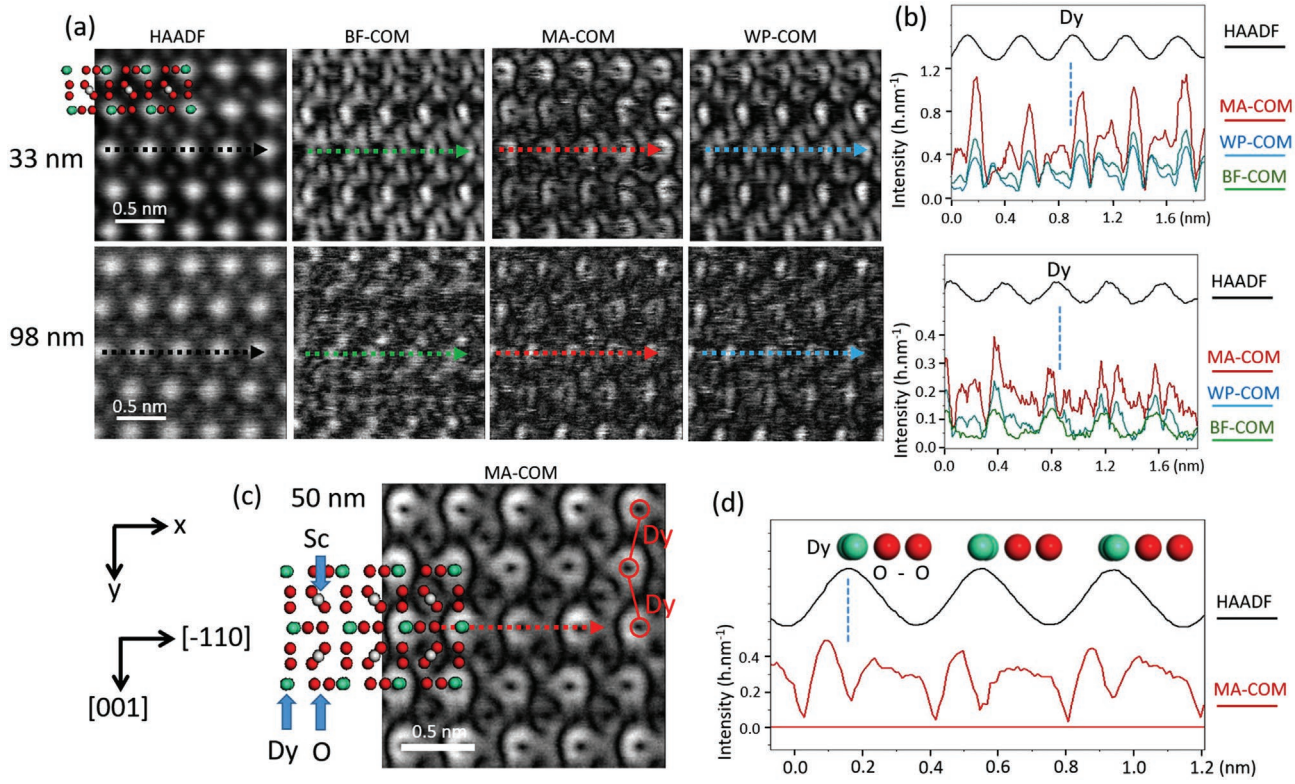


**Figure 2.** a) HAADF-STEM images and intensity of the COM as measured from the BF, MA and WP angular ranges. The sample is oriented along the [1-10] zone axis (Pbnm) and the thicknesses of 33 and 98 nm are, respectively, for the top and bottom part. b) Profiles of the intensity of the HAADF and COM as extracted from the lines indicated on the images of (a). The profiles are for the 33 (top) and 98 nm (bottom) thick areas. c) MA-COM intensity for a 50 nm (left) thick $DyScO_3$ with an improved signal-to-noise ratio (SNR) obtained by an on-line drift cancellation and a multiple data accumulation. d) MA-COM and HAADF profiles for the 50 nm thick sample (position of the profile indicated by the red dotted line in (c)). Please note the strong asymmetry of the MA-COM due to the presence of O-O doublet columns at the right side of the Sr columns.

of columns evidences an almost symmetric HAADF signal and a very asymmetric MA-COM around the Dy columns whose origin is discussed in Figure S4, Supporting Information.

We now turn to the investigation of the electric field across the $SrRuO_3/DyScO_3$ interface. **Figure 3** compares the 4D-STEM results at the $SrRuO_3$/ $DyScO_3$ interface. At first, the STEM images (Figure 3a) and the 4D-STEM data (COM intensity in Figure 3b and intensity component COMx perpendicular to the interface plane in Figure 3c) have been obtained for different angles in the diffraction patterns. In order to have sufficient counting dynamic the images have been acquired in 12 bits depth mode (leading to a 0.9 ms acquisition time) and the scanning step was then limited to 15 pm due to the experimental spatial drift. The BF and ABF images (100 keV) do not have enough spatial resolution to clearly evidence oxygen atoms. The MA-ADF images show stronger white contrast at the SRO interface side and the HAADF contrast is in-line with the expected atomic number of the atoms. The COM intensity evaluated from the BF gives rather "tetragonal" shapes around the atoms (Figure 3b) and its component perpendicular to the interface exhibit a small "decrease then increase" of the electric field toward the DSO at the interface (Figure 3c). For the WP-COM

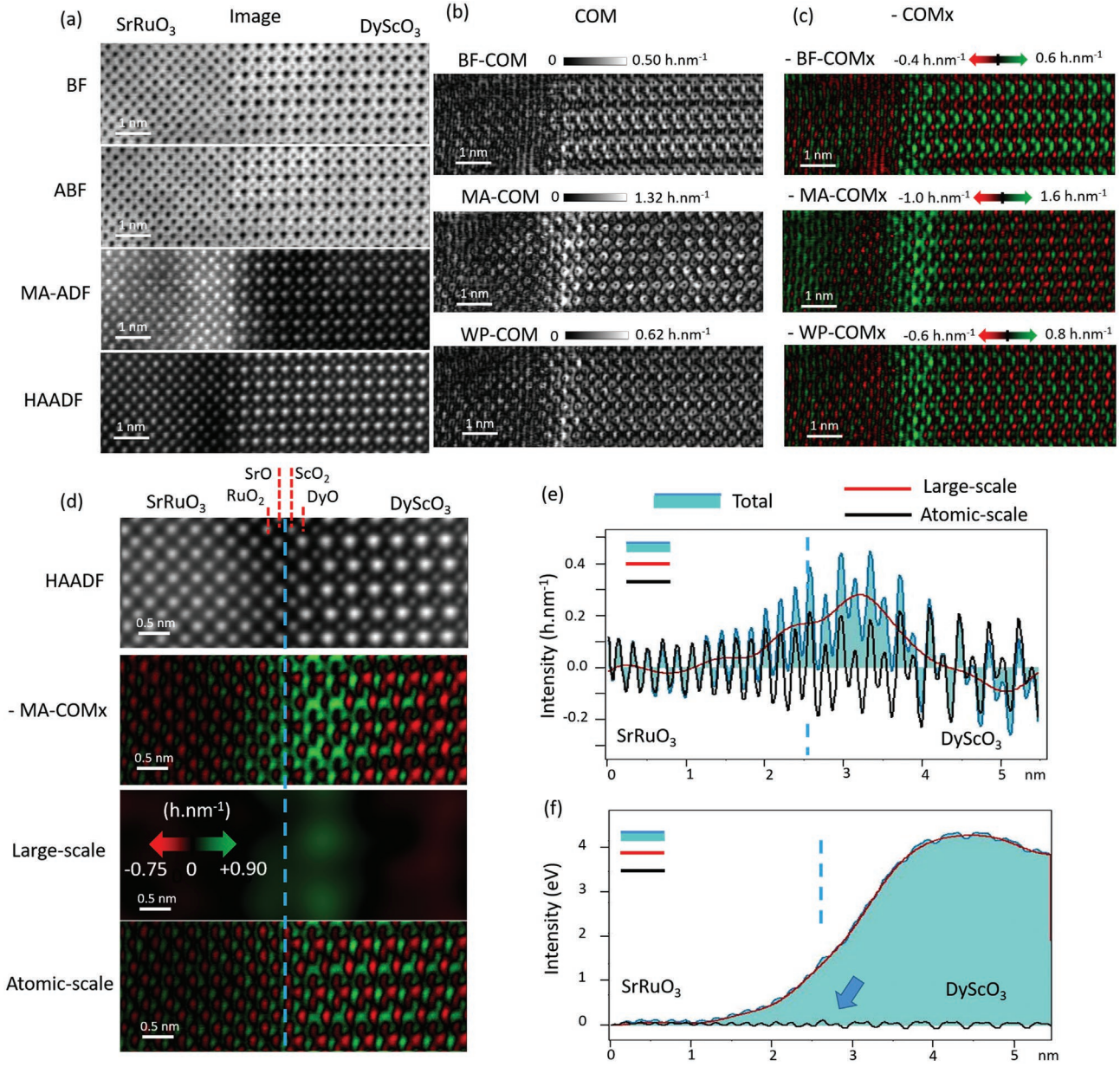


**Figure 3.** a) STEM images of a SRO/DSO interface, b) 4D-STEM COM intensity, and c) components of the COM across the interface, for different angular conditions. d) HAADF-STEM images, COM component across the interface (MA-COMx) and its decomposition between a large-scale and an atomic-scale component. e) Profiles of the total MA-COMx and its two components. f) Profiles of the potentials estimated by integrating the MA-COMx and a thickness normalisation. In (e,f), the cyan plain curve is for the total COM or the total potential. The red lines are for the large-scale components and the dark lines are for the atomic-scale components for COM and potential.

and even more for the MA-COM, the intensity distribution of the COM around the atoms are more spherical, as it was already observed previously. For the large-scale electric field near the interface, they both show an intense electric field pointing toward the DSO (increased of the green contrast). This is also in agreement with the numerical simulations on STO that had evidence that an large-scale electric field was imprinting more deviations to the MA electrons. It is here to note, that the intensity of the MA-ADF STEM images increases at the SRO side, while the MA-COMx intensity is smaller at that side. In brief, more electrons are TDS scattered at the SRO side of the interface but their angular distributions remain symmetric. The disorder that gives more MA-ADF contrast could arise from more chemical disorder or more inter-diffusion at the SRO side (see EELS in Figures S5 and S6, Supporting Information) or from a different vibrational scatterings for the few SRO unit-cells close to the interface. Indeed, transport and magnetic properties are known to behave differently for very thin SRO films (e.g., <4 u.c.[36] that can further couple to phononic modes[37]) and similar behavior might exist for the SRO confined next to the interface. On the other hand, the strong increase of the electric field pointing toward the DSO (green color) is observed from the WP-COMx and even more for the MA-COMx map (Figure 3c). It is also in agreement with the expectation for such interface, where the interfacial electric field is propagating more in the insulating side, that is, the DSO side. Figure 3d shows the MA-COM measured at the interface for a thinner area. The 4D-STEM data quality has also been improved since it is then possible to collect the diffraction with a 1 bit depth allowing rapid multiple acquisitions with online drift compensation. The HAADF obtained during the 4D-STEM acquisition is visible with the corresponding interface plane reconstruction (see the EELS at Figure S6, Supporting Information for its determination). We have then focus on the MA-COMx map and decomposed it by FFT filtering into a large-scale and an atomic-scale component. The corresponding COM profiles are plotted in Figure 3e. The potential profiles (Figure 3f) across the interface have been obtained by integrating these COM profiles assuming that they are representative of the electric fields. As shown before, it might be the case for the large-scale electric field which is deviating the MA-COM electrons. When taking into account the estimated thickness (55 nm), the potential increase from the SRO to the DSO is at ca. 4 eV for the case presented here. Different MA-COM measurements have resulted in potential steps comprised from ca. 3 to 5 eV. Several main sources of errors are present. For instance, the thickness measurements estimated by EELS can suffer rather large uncertainties. Different contributions from the lamella surfaces might also play a role. Small COM offsets from one or the other side of the interface can also easily give a substantial potential offset since it will accumulate over the spatial integration. The field heterogeneity at the interface will also play a role for the TDS electrons that, being scattered at large angles, get delocalized. Nevertheless, the MA-COM seems enough robust for a qualitative measurement of the large-scale potential gradient at the interface. An atomically resolved potential is also obtained from this MA-COM integration and it shows no deviations from the base line confirming that the large-scale electric field contribution has been properly extracted by the FFT filtering. A modification of the shape of that atomic-scale potential is observed near the interface plane (see arrow in Figure 3f) and will be discussed with respect to ab-initio calculation. The EELS investigation of the interface can be seen in Figure S6, Supporting Information and it indicates that the interface is a p-type, id est, the plane termination is $RuO_2$-SrO-$ScO_2$-DyO. Ab-initio calculations have been done with a model comprising two p-type interfaces (see relaxed structural model at **Figure 4**a) and comprising a p- and

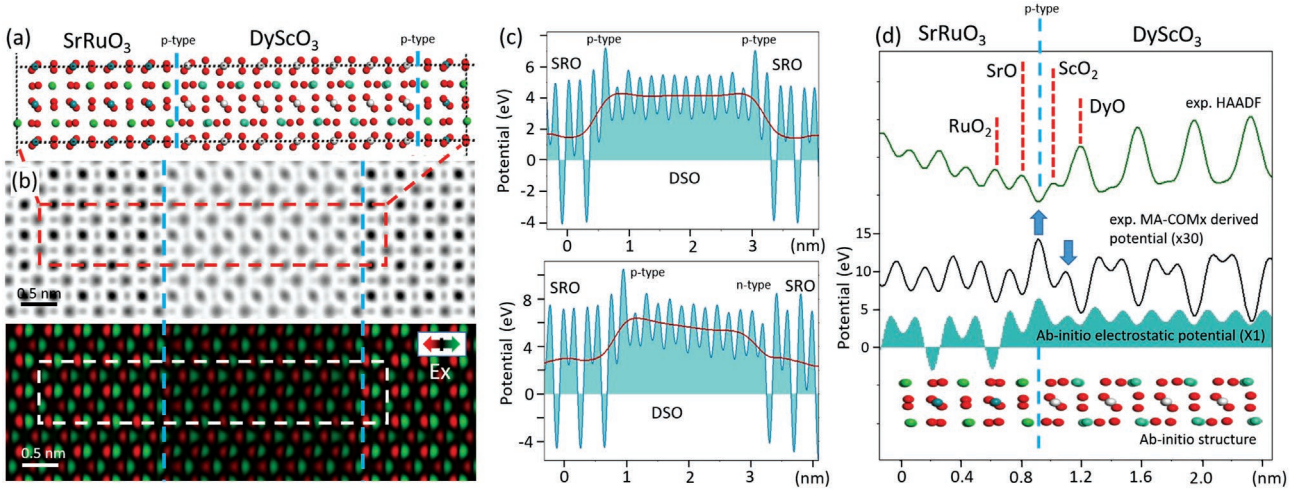


**Figure 4.** a) Ab-initio relaxed structural model of a -p,-p type symmetric SRO/DSO interface, with b) a corresponding electrostatic potential images and electric field component across the interface (Ex). c) ab-initio electrostatic potential profiles for two interfaces models (-p,-p type interface and -p,-n type interface) with two different spatial filtering (red and blue-cyan plain curves). The spatial filtering for the red curve has been set to vanish out the atomic-scale variations of the electrostatic potentials. d) Comparison between 4D-STEM experiments and ab-initio calculation of a n-type interface. HAADF-STEM profile and the 4D-STEM atomic-scale potential profiles are compared to the ab-initio electrostatic potential and the relaxed atomic model. The two blue arrows indicate where the potential increase and decrease in the left and right part of the interfacial unit-cell around the last Sc plane. The Sr, Ru, Sc, Dy and O atoms are, respectively, in green, blue, white, cyan and red. Please note that the ab-initio profile is the electrostatic potential while the 4D-STEM profile is the TDS potential. Both are sensitive to a FE structural distortion at the interface unit cell.

n- type interfaces (model not shown). The electrostatic potential (black and white map) and the corresponding electric field (Ex, red and green map) across the interface can be seen in Figure 4b. The potential increase from the SRO to the DSO is estimated at ca. 3 eV for the p-type interfaces (Figure 4c) that is in rough agreement with the obtained 4D-STEM value. The n-type interface has a smaller potential step. Similar potential step differences have been reported for different plane terminations in the case of SRO/vacuum or SRO/$TiO_2$.[38,39] In the case asymmetric comprising a p- and n- type interfaces, the DSO layer shows a linear potential drop, evidencing the occurrence of an inner electric field in the insulating DSO (SRO being metallic has a constant inner potential). This is also in-line with the 4D-STEM observation of an electric field propagating deeper in the DSO side. These ab-initio peak-to-peak amplitude of the atomically varying potential is in the range of a ten of eV while the potential drop at the interface is of ca. 3 eV (Figure 4c). On the other hand, the atomic-scale TDS potential amplitude as measured by 4D-STEM was order of magnitude lower (Figure 3f) and, as expected for a MA-COM based would not directly related to the electrostatic potential. Nevertheless, due to the shape similarity between the elastic and TDS potential, we investigate if the TDS potential shape of the interface reconstruction might be similar to the electrostatic reconstruction. Figure 4d compares the atomic-scale electrostatic potential shape across the interface obtained by ab-initio and the potential obtained by the 4D-STEM. The 4D-STEM potential show a small increase and decrease in the last unit-cell at the interface. Similar behaviour is observed in the ab-initio profile. It can be interpreted by measuring the atom positions in the ab-initio relaxed model. Far from the interface, the oxygen atoms barycentres are matching with the scandium central atoms, resulting in a symmetric potential distribution within the cell (both experimental and theoretical). It corresponds to the bulk DSO or SRO structural situation where the rotation of oxygen octahedra is non-polar (antiferrodistortive distortion (AFD)) and the potential distribution within the unit cell is symmetric. Close to the interface, an asymmetry is observed in both potentials (electrostatic potential from the ab-initio calculation and TDS based potential from the MA-COM). It is related to a polar displacement of the cation and anion sublattices against one another (ferroelectric distortion (FE)). At the interfacial unit-cell, the average oxygen displacements with respect to the scandium is of 11 pm, moving backward from the interface. This distortion is observed in the DSO side, and is certainly related to presence to a larger-scale electric field at this side of the interface. It indicates here a small ferro-electric type distortion of the interfacial unit cell superimposed with the octahedra rotation of DSO. Competitive or cooperative evolution of the AFD and FE distortions have been reported in $LaAlO_3/SrTiO_3$ interfaces.[40] The present 4D-STEM experiments clearly evidence coexistence of both modes at the insulating side of the interface between metallic and insulating perovskite oxides.

To conclude, 4D-STEM experiment at interfaces can be done including also the MA-COM component. This latter component had given a fair estimation of the large-scale electric field at the interface for a rather thick sample. It has also given an atomic-scale TDS potential whose shape was sensitive to minute atomic displacement near the interface, that can be further interpreted with the help of ab-initio relaxed structure. Presence of local electric dipoles have then been observed with unit-cell resolution revealing unambiguously the balance evolution between antiferrodistortive and ferroelectric instabilities at the interface between metallic and insulating oxides.

## 3. Experimental Section

*$SrTiO_3$ 4D-STEM Simulations:*4D-STEM data of $SrTiO_3$ without external electric field have been computed by multi-slice software QSTEM.[41] The probe is set with 100 keV accelerating voltage, convergence angle of 30 mrad, focus at the entrance plane. Typical slice thickness of 0.1 nm is used and thermal diffuse scattering is included through multiple calculations of the probe propagation with different sets of thermally displaced structural inputs. The COM and phases in Figure 1 are calculated with the py4DSTEM library.[9] The averaged COM of the Sr and O columns in Figure 1b is calculated by averaging the values within the circular areas indicated in Figure 1a. 4D-STEM data of $SrTiO_3$ with the presence of an external electric field have been computed by multi-slice software abTEM.[33] The probe is set with 100 keV accelerating voltage, convergence angle of 30 mrad, focus at the entrance plane comparable to the experimental conditions. It is also checked that results obtained without an external field at 100 keV (behavior of the BF-COM, MA-COM, and WP-COM with thickness) with abTEM was comparable to the one obtained previously by QSTEM. Furthermore, similar simulations have been done with a probe set with 200 keV accelerating voltage and convergence angle of 23 mrad (Figure S1, Supporting Information).

*High Resolution STEM, EELS, 4D-STEM:*STEM experiments have been done using a Cs corrected NION microscope. All experiments have been done at 100 keV with a probe-current of ca. 10 pA and convergence semi-angles of 30 mrad. A MerlinEM in a 4×1 configuration (1024 × 256) has been installed on a Gatan ENFINA spectrometer mounted on the microscope.[42] The EELS spectra are obtained using the full 4 × 1 configuration and the 4D-STEM by selecting only one of the chips (256 × 256 pixels). For 4D-STEM, the EELS spectrometer is set into non-energy-dispersive trajectories. Detectors have been used with different bit counting depths (b1, b6, b12, b24). The 1- bit counting depth is resulting in a saturated BF disk that is not a limitation for MA-COM measurement and allow fastest measurement. On-line spatial drift correction of the EELS and 4D-STEM datasets have been used. The spatial drift is estimated on-line by the HAADF images acquired simultaneously with the 3D or 4D datasets (spectrum imaging – 3D dataset or diffraction – imaging 4D dataset). The cross-correlations between successive HAADF images are used to estimate the drift occurring during each scan. The first two datasets enable a first estimation of the spatial drift and then the probe scanning array is adapted to anticipate and cancel the drift at every probe positions of the following datasets acquisitions with an accuracy that can be as small as 1/16 of the probe step. The EELS and 4D-STEM datasets could then be summed on-line, limiting the total amount of stored data Throughout the article, the COM direction is always displayed as -COM, in order to ease a comparison with the electric field direction. The COM unit is "$h.nm^{-1}$". A COM deviation of 1 mrad corresponds to a lateral momentum of 0.27 $h.nm^{-1}$ (at 100 keV) and of 0.40 $h.nm^{-1}$ (at 200 keV). When converted in $E\Delta z$, 1 mrad COM is 184 V (at 100 keV) and 344 V (at 200 keV). Hence, a 100keV electron propagating within a lateral electric field of $E = 5\ V\ nm^{-1}$ along a thickness $\Delta z = 10$ nm will acquire 0.27 mrad of deviation. The thicknesses have been estimated by EELS using the log-ratio method[43] and a mean free path estimated according to Malis et al.[44] Mean inelastic free paths of ca. 53 nm and 58 nm have been estimated for, respectively, DSO and STO. Experimental EELS spectra have been obtained with a small dispersion allowing the collection from the zero-loss peak (ZLP) to ca. 1000 eV loss. In order to avoid saturation effects a 24 bits counting depth has been used and a good linearity of the counting has been maintained by keeping an electron flux at every pixel of the MerlinEM detector below 1e5 electrons per second (even for the most intense part of the ZLP).

*Ab-Initio Simulation of DSO and of SRO/DSO Interfaces:*Ab-initio calculations based on density functional theory (DFT) in a plane-wave pseudopotential approach as implemented in QUANTUM ESPRESSO were done.[45,46] Structural relaxations have be done with ultrasoft pseudopotential, including, respectively, 6, 8, 10, 11 and 12 valence electrons for O, Ru, Sr, Sc and Dy with an energy cutoff of 50 Ry for the plane-wave basis expansion.[47] $DyScO_3$ bulk (40 atoms) has been converged with $4 \times 4 \times 4$ k-points mesh. Interface models comprise 240 atoms and the charge density has been converged with $4 \times 4 \times 1$ k-points mesh. For potential and electric field calculation, an energy cut-off above 100 Ry is used for the plane-wave basis expansion with corresponding pseudopotentials. For comparison with the 4D-STEM data, the exchange and correlation contributions are removed from the total potential. The electrostatic potentials are expressed with the dimension of an energy (e×V), id est, a minimum is observed at the nuclei positions.

## Supporting Information

Supporting Information is available from the Wiley Online Library or from the author.

## Acknowledgements

The authors are grateful to Pr. A. Zobelli (Orsay, France) for fruitful discussions and for the help on the ab-initio calculation and to Dr. M. Tencé (Orsay, France) for the integration of the MerlinEM detector (Quantum Detectors Ltd) into a spectrum-imaging EELS and a 4D-STEM acquisition system. Dr C. Lichtensteiger and Dr M. Hadjimichael (Geneva, Switzerland) are also acknowledged for providing the DSO/SRO sample. This research was supported by the ESTEEM-3 project (H2020-EU, grant agreement ID 823717), the oxide based spinorbitronic (OISO) project (ANR-17-CE24-0026) and the Transmission Electron Microscopy at Palaiseau Orsay Saclay (TEMPOS) project (ANR-10-EQPX-0050). Q.J. acknowledges support from the University of Chinese Academy of Sciences (UCAS) Joint PhD Training Program.

## Conflict of Interest

The authors declare no conflict of interest.

## Data Availability Statement

The data that support the findings of this study are available from the corresponding author upon reasonable request.

## Keywords

ab-initio calculation, interface, nanostructure, oxide, potential well, STEM

Received: October 2, 2022
Revised: November 21, 2022
Published online: December 16, 2022

[1] T. Yajima, Y. Hikita, M. Minohara, C. Bell, J. A. Mundy, L. F. Kourkoutis, D. A. Muller, H. Kumigashira, M. Oshima, H. Y. Hwang, *Nat. Commun.* **2015**, *6*, 6759.
[2] S. Gariglio, A. D. Caviglia, J.-M. Triscone, M. Gabay, *Rep. Prog. Phys.* **2019**, *82*, 012501.
[3] A. B. Yankovich, B. Berkels, W. Dahmen, P. Binev, S. I. Sanchez, S. A. Bradley, A. Li, I. Szlufarska, P. M. Voyles, *Nat. Commun.* **2014**, *5*, 4155.
[4] S. D. Findlay, N. Shibata, H. Sawada, E. Okunishi, Y. Kondo, T. Yamamoto, Y. Ikuhara, *Appl. Phys. Lett.* **2009**, *95*, 191913.
[5] R. Aso, D. Kan, Y. Shimakawa, H. Kurata, *Sci. Rep.* **2013**, *3*, 2214.
[6] X. Li, I. Lindfors-Vrejoiu, M. Ziese, A. Gloter, P. A. van Aken, *Sci. Rep.* **2017**, *7*, 40068.
[7] B. Shen, X. Chen, K. Shen, H. Xiong, F. Wei, *Nat. Commun.* **2020**, *11*, 2692.
[8] Z. Chen, Y. Jiang, Y.-T. Shao, M. E. Holtz, M. Odstrčil, M. Guizar-Sicairos, I. Hanke, S. Ganschow, D. G. Schlom, D. A. Muller, *Science* **2021**, *372*, 826.
[9] B. H. Savitzky, S. E. Zeltmann, L. A. Hughes, H. G. Brown, S. Zhao, P. M. Pelz, T. C. Pekin, E. S. Barnard, J. Donohue, L. Rangel DaCosta, E. Kennedy, Y. Xie, M. T. Janish, M. M. Schneider, P. Herring, C. Gopal, A. Anapolsky, R. Dhall, K. C. Bustillo, P. Ercius, M. C. Scott, J. Ciston, A. M. Minor, C. Ophus, *Microsc. Microanal.* **2021**, *27*, 712.
[10] O. Cretu, A. Ishizuka, K. Yanagisawa, K. Ishizuka, K. Kimoto, *ACS Nano* **2021**, *15*, 5316.
[11] C. Addiego, W. Gao, X. Pan, *Ultramicroscopy* **2020**, *208*, 112850.
[12] S. Fang, Y. Wen, C. S. Allen, C. Ophus, G. G. D. Han, A. I. Kirkland, E. Kaxiras, J. H. Warner, *Nat. Commun.* **2019**, *10*, 1127.
[13] R. Ishikawa, S. D. Findlay, T. Seki, G. Sánchez-Santolino, Y. Kohno, Y. Ikuhara, N. Shibata, *Nat. Commun.* **2018**, *9*, 3878.
[14] W. Gao, C. Addiego, H. Wang, X. Yan, Y. Hou, D. Ji, C. Heikes, Y. Zhang, L. Li, H. Huyan, T. Blum, T. Aoki, Y. Nie, D. G. Schlom, R. Wu, X. Pan, *Nature* **2019**, *575*, 480.
[15] J. A. Hachtel, J. C. Idrobo, M. Chi, *Adv. Struct. Chem. Imag.* **2018**, *4*, 10.
[16] K. Müller-Caspary, F. F. Krause, F. Winkler, A. Béché, J. Verbeeck, S. Van Aert, A. Rosenauer, *Ultramicroscopy* **2019**, *203*, 95.
[17] R. Close, Z. Chen, N. Shibata, S. Findlay, *Ultramicroscopy* **2015**, *159*, 124.
[18] K. Müller-Caspary, M. Duchamp, M. Rösner, V. Migunov, F. Winkler, H. Yang, M. Huth, R. Ritz, M. Simson, S. Ihle, H. Soltau, T. Wehling, R. E. Dunin-Borkowski, S. Van Aert, A. Rosenauer, *Phys. Rev. B* **2018**, *98*, 121408.
[19] K. Müller, F. F. Krause, A. Béché, M. Schowalter, V. Galioit, S. Löffler, J. Verbeeck, J. Zweck, P. Schattschneider, A. Rosenauer, *Nat. Commun.* **2014**, *5*, 5653.
[20] N. Shibata, S. D. Findlay, H. Sasaki, T. Matsumoto, H. Sawada, Y. Kohno, S. Otomo, R. Minato, Y. Ikuhara, *Sci. Rep.* **2015**, *5*, 10040.
[21] I. MacLaren, L. Wang, D. McGrouther, A. J. Craven, S. McVitie, R. Schierholz, A. Kovács, J. Barthel, R. E. Dunin-Borkowski, *Ultramicroscopy* **2015**, *154*, 57.
[22] T. Grieb, F. F. Krause, K. Müller-Caspary, R. Ritz, M. Simson, J. Schörmann, C. Mahr, J. Müßener, M. Schowalter, H. Soltau, M. Eickhoff, A. Rosenauer, *Ultramicroscopy* **2021**, *228*, 113321.
[23] K. Müller-Caspary, T. Grieb, J. Müßener, N. Gauquelin, P. Hille, J. Schörmann, J. Verbeeck, S. Van Aert, M. Eickhoff, A. Rosenauer, *Phys. Rev. Lett.* **2019**, *122*, 106102.
[24] C. Yang, Y. Wang, W. Sigle, P. A. van Aken, *Nano Lett.***2021**, acs.nanolett.1c02960.
[25] J.-Y. Chauleau, T. Chirac, S. Fusil, V. Garcia, W. Akhtar, J. Tranchida, P. Thibaudeau, I. Gross, C. Blouzon, A. Finco, M. Bibes, B. Dkhil, D. D. Khalyavin, P. Manuel, V. Jacques, N. Jaouen, M. Viret, *Nat. Mater.* **2020**, *19*, 386.
[26] S. Fusil, J.-Y. Chauleau, X. Li, J. Fischer, P. Dufour, C. Leveille, C. Carrétéro, N. Jaouen, M. Viret, A. Gloter, V. Garcia, *Adv. Electron. Mater.* **2022**, 112912.
[27] R. Egoavil, H. Tan, J. Verbeeck, S. Bals, B. Smith, B. Kuiper, G. Rijnders, G. Koster, G. Van Tendeloo, *Appl. Phys. Lett.* **2013**, *102*, 223106.

[28] A. B. Mei, S. Saremi, L. Miao, M. Barone, Y. Tang, C. Zeledon, J. Schubert, D. C. Ralph, L. W. Martin, D. G. Schlom, *APL Mater.* **2019**, *7*, 111101.
[29] W. Lu, W. Song, P. Yang, J. Ding, G. M. Chow, J. Chen, *Sci. Rep.* **2015**, *5*, 10245.
[30] F. Winkler, J. Barthel, R. E. Dunin-Borkowski, K. Müller-Caspary, *Ultramicroscopy* **2020**, *210*, 112926.
[31] L. J. Allen, C. J. Rossouw, *Phys. Rev. B* **1990**, *42*, 11644.
[32] M. C. Cao, Y. Han, Z. Chen, Y. Jiang, K. X. Nguyen, E. Turgut, G. Fuchs, D. A. Muller, *Microsc. Microanal.***2017**, *23*, 444, arXiv:1711.07470 [physics].
[33] J. Madsen, T. Susi, *Open Res. Eur.* **2021**, *1*, 13015.
[34] T. Susi, J. Madsen, U. Ludacka, J. J. Mortensen, T. J. Pennycook, Z. Lee, J. Kotakoski, U. Kaiser, J. C. Meyer, *Ultramicroscopy* **2019**, *197*, 16.
[35] J. Chapman, I. McFadyen, S. McVitie, *IEEE Trans. Magn.* **1990**, *26*, 1506.
[36] S. Pang, *AM* **2017**, *47*, 187.
[37] S. G. Jeong, S. Y. Lim, J. Kim, S. Park, H. Cheong, W. S. Choi, *Nanoscale* **2020**, *12*, 13926.
[38] V. Sampath Kumar, M. K. Niranjan, *J. Appl. Phys.* **2014**, *115*, 173705.
[39] N. Ferdous, E. Ertekin, *J. Appl. Phys.* **2016**, *120*, 035302.
[40] T. Min, W. Choi, J. Seo, G. Han, K. Song, S. Ryu, H. Lee, J. Lee, K. Eom, C.-B. Eom, H. Y. Jeong, Y.-M. Kim, J. Lee, S. H. Oh, *Sci. Adv.s* **2021**, *7*, 17.
[41] C. T. Koch, Ph.D. thesis, Arizona State University **2002**.
[42] M. Tencé, J.-D. Blazit, X. Li, M. Krajnak, E. N. del Busto, R. Skogeby, L. Cambou, M. Kociak, O. Stephan, A. Gloter, *Microsc. Microanal.* **2020**, *26*, 1940.
[43] R. Egerton, S. Cheng, *Ultramicroscopy* **1987**, *21*, 231.
[44] T. Malis, S. C. Cheng, R. F. Egerton, *J. Elec. Microsc. Tech.* **1988**, *8*, 193.
[45] P. Giannozzi, O. Baseggio, P. Bonfá, D. Brunato, R. Car, I. Carnimeo, C. Cavazzoni, S. de Gironcoli, P. Delugas, F. Ferrari Ruffino, A. Ferretti, N. Marzari, I. Timrov, A. Urru, S. Baroni, *J. Chem. Phys.* **2020**, *152*, 154105.
[46] P. Giannozzi, S. Baroni, N. Bonini, M. Calandra, R. Car, C. Cavazzoni, D. Ceresoli, G. L. Chiarotti, M. Cococcioni, I. Dabo, A. Dal Corso, S. de Gironcoli, S. Fabris, G. Fratesi, R. Gebauer, U. Gerstmann, C. Gougoussis, A. Kokalj, M. Lazzeri, L. Martin-Samos, N. Marzari, F. Mauri, R. Mazzarello, S. Paolini, A. Pasquarello, L. Paulatto, C. Sbraccia, S. Scandolo, G. Sclauzero, A. P. Seitsonen, et al., *J. Phys.: Condens. Matter* **2009**, *21*, 395502.
[47] A. Dal Corso, *Comput. Mater. Sci.* **2014**, *95*, 337.